

THE SPECTACULAR RADIO-NEAR-IR-X-RAY JET OF 3C 111: X-RAY EMISSION MECHANISM AND JET KINEMATICS

DEVON CLAUTICE¹, ERIC S. PERLMAN¹, MARKOS GEORGANOPOULOS², MATTHEW L. LISTER³, FRANCESCO TOMBESI^{4,5}, MIHAI CARA⁶, HERMAN L. MARSHALL⁷, BRANDON HOGAN³, DEMOS KAZANAS⁵

Draft version November 8, 2018

ABSTRACT

Relativistic jets are the most energetic manifestation of the active galactic nucleus (AGN) phenomenon. AGN jets are observed from the radio through gamma-rays and carry copious amounts of matter and energy from the sub-parsec central regions out to the kiloparsec and often megaparsec scale galaxy and cluster environs. While most spatially resolved jets are seen in the radio, an increasing number have been discovered to emit in the optical/near-IR and/or X-ray bands. Here we discuss a spectacular example of this class, the 3C 111 jet, housed in one of the nearest, double-lobed FR II radio galaxies known. We discuss new, deep *Chandra* and *HST* observations that reveal both near-IR and X-ray emission from several components of the 3C 111 jet, as well as both the northern and southern hotspots. Important differences are seen between the morphologies in the radio, X-ray, and near-IR bands. The long (over 100 kpc on each side), straight nature of this jet makes it an excellent prototype for future, deep observations, as it is one of the longest such features seen in the radio, near-IR/optical and X-ray bands. Several independent lines of evidence, including the X-ray and broadband spectral shape as well as the implied velocity of the approaching hotspot, lead us to strongly disfavor the EC/CMB model and instead favor a two-component synchrotron model to explain the observed X-ray emission for several jet components. Future observations with *NuSTAR*, *HST*, and *Chandra* will allow us to further constrain the emission mechanisms.

1. INTRODUCTION

One of the milestone discoveries of *Chandra* was the X-ray emission from nearly 100 quasar and radio galaxy jets, as well as their hotspots⁸. The latter are high brightness regions where the jets collide with the intergalactic medium. In the radio and optical, the emission from these sites is synchrotron in nature. This guarantees the presence of X-ray emission, via the Synchrotron Self Compton (SSC) process. The discrepancy between the observed X-ray fluxes and the predictions of SSC models is often glaring (e.g., Schwartz et al. 2000; Wilson et al. 2001; Sambruna et al. 2004; Marshall et al. 2005), with the X-rays commonly being orders of magnitude brighter than the SSC prediction if equipartition magnetic fields are assumed. Tavecchio et al. (2000) and Celotti et al. (2001) proposed to explain this excess X-ray emission as external Compton (EC) scattering of cosmic microwave background (CMB) photons by the jet's relativistic electrons. This requires jets with bulk Lorentz factor $\Gamma \sim 10$ that are oriented close to the line of sight for nearly their entire length. Alternatively (Der-

mer & Atoyan 2002), the X-rays may be synchrotron emission from high energy electrons suffering Compton losses in the Klein-Nishina regime. These particles are often required to be in a separate high-energy population (Hardcastle et al. 2004; Hardcastle 2006). In this case, the X-ray and optical emission require *in situ* particle acceleration, as the radiating particles have lifetimes of a few to hundreds of years, much shorter than the particle's time to travel down the jet. Those emissions would then provide an excellent probe of the physics in jet regions where particle acceleration is happening. A third model (upstream Compton, Georganopoulos & Kazanas 2003), proposes a decelerating jet, with electrons in the faster, upstream flow scattering photons produced in the slow downstream flow, thus contributing to the X-ray emission.

Discriminating between these models relies on several diagnostics, including component spectral energy distributions (SEDs) and differences between radio and X-ray jet morphology (Jester et al. 2006; Kharb et al. 2012)). We have proposed two diagnostics that can rule out the EC/CMB model. The first of these (Krawczynski 2012; Poutanen 1993) relies on the fact that except for scatterings from low-energy particles ($\gamma \sim 1$) inverse-Comptonized CMB radiation should be unpolarized, reflecting the unpolarized nature of the seed photon population. This diagnostic was first used by Cara et al. (2013) to almost completely rule out the EC/CMB model for one quasar jet, PKS 1136-135. Another diagnostic (Georganopoulos et al. 2006) relies on the fact that the observed synchrotron emission at IR and lower energies must also be Comptonized, resulting in a minimum level of GeV gamma-ray emission. This has ruled out the EC/CMB model for the jets of 3C 273 and PKS 0637-752 (Meyer & Georganopoulos 2014; Meyer et al.

¹ Department of Physics and Space Sciences, Florida Institute of Technology, 150 W. University Blvd., Melbourne, FL 32901, USA

² Department of Physics, University of Maryland – Baltimore County, 1000 Hilltop Circle, Baltimore, MD 21250, USA

³ Department of Physics and Astronomy, Purdue University, 525 Northwestern Avenue, West Lafayette, IN 47907, USA

⁴ Department of Astronomy, University of Maryland, College Park, MD 20742-2421

⁵ NASA's Goddard Space Flight Center, Astrophysics Science Division, Code 663, Greenbelt, MD 20771, USA

⁶ Space Telescope Science Institute, 3700 San Martin Drive, Baltimore, MD 21218, USA

⁷ Kavli Institute for Astrophysics and Space Research, Massachusetts Institute of Technology, Cambridge, MA 02139, USA

⁸ see e.g., <https://hea-www.harvard.edu/XJET/>

2015)). Finally, in a few FR IIs (e.g., Pictor A, Hardcastle et al. (2016); Gentry et al. (2015); Marshall et al. (2010)) that are viewed at larger angles, the broadband SED even suggests synchrotron emission without requiring a separate, high-energy electron population.

With all of these different possibilities, one of the most basic needs for investigating models of both jet emission and physics is to find ideal testing grounds. Only a very few prototype jets, that are bright in several bands at low redshifts, and minimally bent, are known. Here we discuss a new, prototype jet.

3C 111 is a powerful FR II radio galaxy (Fanaroff & Riley 1974) at $z = 0.0485$ (Hewitt & Burbidge 1991). Our *HST* images (§§2-3) show that the host galaxy is a bright giant elliptical with somewhat distorted outer isophotes, and several prominent companions within 50 kpc. On parsec scales, VLBI observations show component speeds as high as $8c$ in the approaching, northern jet (Lister et al. 2013). Shallow, 10 ks *Chandra X-ray Observatory* survey observations by Hogan et al. (2010) revealed X-ray emission from three knots in the northern jet (which we call K30, K61 and K97) and the northern hotspot (NHS). The jet is extremely long (nearly 4 arcminutes) and its host galaxy resides in a rich optical environment. Here we discuss the results of new, deep observations with both *Chandra* and the *Hubble Space Telescope* (HST). These observations not only confirm the results of Hogan et al. (2010) but also reveal near-IR and X-ray emission from several components in the 3C 111 jet, as well as the southern (receding) hotspot.

This paper is laid out as follows: In Section 2, we describe our observations and data reduction methods. Section 3 shows the results and discusses the broadband spectrum of the jet components. We close in Section 4 by stating our conclusions. Throughout this paper we assume $\Omega_m = 0.27$, $\Omega_\Lambda = 0.73$, $\Omega_r = 0$ and $H_0 = 71 \text{ km s}^{-1} \text{ Mpc}^{-1}$.

2. OBSERVATIONS AND DATA REDUCTIONS

2.1. *Chandra* Observations

Chandra has observed 3C 111 three times with the ACIS-S. In 2008, a shallow, 10 ks survey observation (dataset 701719) was taken (Hogan et al. 2010), which discovered the X-ray emission from the jet. On 10-11 January 2013, we obtained much deeper observations (dataset 702798), for a total on-source time of 127 ks. These observations were gathered using alternating exposure mode, with interleaved frame times of 1.5s ($\times 4$) and 0.3s ($\times 1$) during each cycle. This was done in order to enable us to minimize the effect of pileup in the region of the quasar nucleus, while at the same time keeping the majority of the time optimized for detection of fainter sources in a broader field. It reduced efficiency by 15%, giving us a total exposure time of 92 ks (1.5s frame time only), but allowed us to discriminate inner jet knots from emission due to the AGN in the innermost 10 arcseconds, where pileup is a factor, by using the 0.3s frame time data (17 ks exposure time). These observations were augmented on 4-5 November 2014 by ACIS/HETG observations (150 ks, PI F. Tombesi, dataset 703007).

All observations were reduced in CIAO version 4.8.0, using CALDB v. 4.7.0, with standard screening criteria and calibration files provided by the *Chandra X-*

Ray Center. Pixel randomization was removed, and only events in grades 0, 2 - 4, and 6 were retained. We also checked for flaring background events. No significant flaring events were found, so that we did not have to filter by time. We subsampled the native *Chandra* resolution by 4, leading to a pixel scale of 0.123 arcsec/pixel. Datasets 702798 and 703007 were combined to obtain the images discussed in this paper. We chose not to incorporate the much shallower dataset 701719 into that analysis because of its poor statistics. To show the extended structure, we smoothed the X-ray image adaptively using the CIAO task *csmooth*, smoothing only below a minimum significance of 4.⁹

2.2. *HST* Observations

HST observed 3C 111 on 30 January 2013 for three orbits, using the Wide-field Camera 3 (WFC3). Images were gathered both in the UVIS channel using the F850LP filter (1 orbit) and in the IR channel using the F160W filter (2 orbits). Because of the size of the 3C 111 jet-hotspots system, we restricted *HST*'s orientation so that the jet fell along a chip diagonal in both observations. Unfortunately for ease of scheduling we had to leave a 10-degree allowance on the allowed position angle (PA), and the PA that was used placed emission from the NHS at the edge of the field of the UVIS/F850LP observation. To compensate for this, we located archival observations obtained on 26 February 1996 with the Wide-Field and Planetary Camera 2 (WFPC 2) with the F791W filter (PI Meisenheimer). These latter observations include only the northern hotspot and some of the northern jet. Because of the small field of view, two pointings were necessary in the IR channel, while one pointing was deemed adequate in the UVIS. In addition, we used a standard, 2-position dither pattern at each location in each band. This, combined with the multiple readouts, was more than adequate to remove bad pixels and cosmic rays in the IR/F160W observation, but in the UVIS/F850LP observation it was not adequate, and there were a significant number of pixels that had cosmic ray strikes in both images. In addition to the above there exist two shorter observations obtained with NICMOS and WFC2 (PI Sparks). Table 1 gives details of all *HST* observations.

All *HST* images were re-calibrated in PYRAF using the most up-to-date reference files (i.e., flat field, distortion correction table, etc.) obtained from the STScI Calibration Database system. We corrected for charge transfer efficiency (CTE) effects in the UVIS/F850LP data using the recipe of Anderson et al. (2012) and in the WFPC2 data using the recipe of Dolphin (2000) and Riess (2000). In the UVIS/F850LP data we also pre-processed the data using L.A. Cosmic¹⁰ (van Dokkum 2001) prior to drizzling. This significantly decreased the number of cosmic rays affecting the final image. We used the *Astrodrizzle* task (Gonzaga et al. 2012) from the STSCI_PYTHON package to drizzle-combine the images for each of the two filter combinations. Besides combining the images, *Astrodrizzle* distortion-corrects the images, performs image flat-fielding, cosmic-ray rejection,

⁹ This smoothed image was not used for scientific measurements, but is useful for illustrative purposes.

¹⁰ see <http://www.astro.yale.edu/dokkum/lacosmic/>

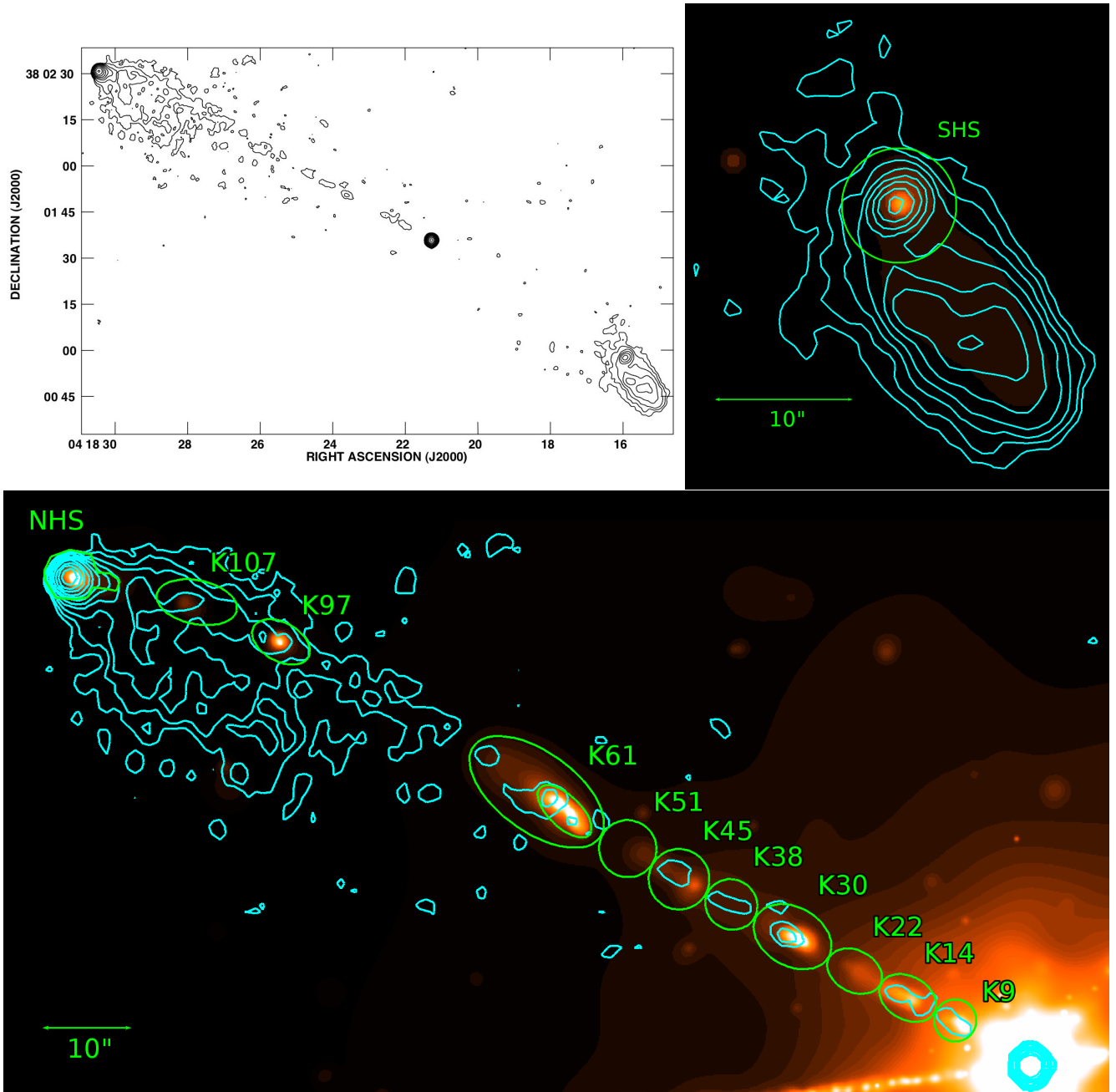


Figure 1. 3C 111, as seen in a 1989 8 GHz VLA observation (top left, Leahy et al. 1997), and a deep *Chandra* X-ray observation. The *Chandra* image, shown at top right and bottom, shows the X-ray image displayed with a heat scale and radio emission overlaid as cyan contours. The *Chandra* image shows emission from eight jet regions (named in green), as well as the northern and southern hotspots (NHS and SHS). Also shown in green are the flux extraction regions for each knot region. Note that significant differences exist between the morphology seen in the two bands. See §§2, 3 for discussion.

image alignment, and other tasks. Prior to any analysis, the HST data had to be galaxy-subtracted. This was done using the tasks `ellipse` and `bmodel`. The model fitting was done iteratively, excluding nearby stars and galaxies (note that 3C 111 lies in a fairly dense cluster of galaxies).

Local background regions were used to determine the blank sky noise emission for each source aperture. Sigma clipping was used to eliminate any pixel values that deviated beyond 3 sigma from the median. Photon noise was estimated by multiplying the weight map created by

`Astrodrizzle` with our science image (in counts/second) to obtain the number of counts in each sky-subtracted source region. Read noise was taken from the header values in each image; dark current was estimated from the dark reference file indicated in the header.

Aperture photometry was done on the images using the apertures shown in Figure 1. Aperture correction was done following the recommendations of the WFC3 Data Handbook (Rajan et al. 2011), while for the WFPC2 dataset it was done following Holtzman et al. (1995). Conversion to flux units was performed by multiplying

Table 1
HST Observations of 3C 111

Date	Program	Instrument	Band	λ_{pivot} (nm)	width (nm)	$T_{int}(s)$
30/01/2013	13114	WFC3/UVIS	F850LP	916.6	118.2	2534
30/01/2013	13114	WFC3/IR	F160W	1536.9	268.3	2606 ^a
26/02/1996	5931	WFPC2	F791W	788.1	123.1	53400 ^b
08/12/2004	10173	NICMOS/NIC2	F160W	1600	400	1152 ^c
19/11/1995	5476	WFPC2	F702W	691.9	138.5	600 ^d

^a Two pointings. Integration time is per pointing.

^b Field does not include host galaxy or optically seen part of jet.

^c Field includes only one knot region (K9) and image is not deep enough to confirm its detection.

^d Very shallow image, does not show jet, not used.

image data in electrons/s by the corresponding λ values for all images. 3C 111 is at a low galactic latitude ($b_{II} = 8.8^\circ$), relatively near the Taurus molecular cloud (the nearest large star-forming region in our Galaxy). Ungerer et al. (1985), in their detailed optical and radio study, pointed out that the region of the cloud in front of 3C 111 is not the densest part (see Figure 3 of Ungerer et al. 1985). This result is also supported by the results of the XMM-Newton Extended Survey of the Taurus Molecular Cloud project (Güdel et al. 2007). Due to the presence of this molecular cloud, galactic extinction is unfortunately high, with $A_V = 4.5$ mag assuming a standard $R_V = 3.1$ (Schlafly & Finkbeiner 2011; Schlegel, Finkbeiner & Davis 1998). We note that Meisenheimer et al. (1997) used a much lower value for the extinction to 3C 111, stemming from the earlier survey of Burstein & Heiles (1982) (see also §3).

3. RESULTS

The 3C 111 jet can be seen across the electromagnetic spectrum, from the radio through the X-rays. In Figure 1, we show our deep *Chandra* imaging of 3C 111, along with archival VLA imaging (Leahy et al. 1997). X-ray emission is evident in at least 8 jet regions, plus the northern and southern hotspot. This emission is also seen in the near-IR, as shown in Figure 2, which shows close-ups of three jet regions in the F160W image, respectively the northern hotspot, inner jet and southern hotspots. The near-IR image shows emission from most, but not all X-ray emitting jet regions. In the F850LP and F791W images, the only jet or jet-related emission that can be seen comes from the northern hotspot. This is likely a result of the high Galactic extinction towards 3C 111. Most of the panels in Figures 1 and 2 show one image as greyscale and another as contours, allowing us to compare the morphology in different bands. To aid in this comparison, we named the northern jet features using the distance in arcseconds from the nucleus. Thus, as an example, knot K14 has its flux maximum $14''$ from the nucleus.

3.1. Jet Morphology

There is significant evidence of differences between the radio, near-IR and X-ray morphology, as seen in Figures 1 and 2, as well as in Figure 3, which shows the profile of relative flux (each normalized to 1 at an arbitrary point) along the jet in the *Chandra*, F160W, and VLA images. We note that there are strong differences between the radio, near-IR and X-ray fluxes. The near-IR and X-ray morphology are discussed in detail here. The radio mor-

phology will be discussed in more detail in a future paper, where we also discuss follow-on deep JVLA observations. In the next sub-section, we will discuss the spectral energy distribution of the jet features, including the X-ray and optical spectral indices for the knots where it was possible to extract such information. In registering the three data sets to a common frame of reference, we assumed the VLA map to be the fiducial, adhering to the usual IAU standard. The *HST* images were registered to this frame by hand, as the Guide Star Catalog alignment always has errors of near arcsecond level, assuming that the optical and radio AGN core positions were identical. To register the *Chandra* data to this frame, we followed the CIAO thread ‘‘Correcting Absolute Astrometry’’, using CIAO task *wavdetect* to match sources in the 2MASS catalog in the *Chandra* images. This yielded a final offset of about $0.2''$ from the radio. We also merged the data from datasets 702798 and 703007 using *reproject_obs* in CIAO. Following this, the 1σ errors in the positions from the *HST* image are $< 0.02''$, while those in the X-ray image are $\pm 0.16''$ relative to the radio frame of reference according to Rots & Budavari (2011), although to be conservative for this purpose we used $0.3''$.

Components within $\sim 20''$ of the nucleus have flux profiles in the X-rays that are mixed with that of the unresolved nuclear source due to the *Chandra* PSF (see Fig. 3), and are somewhat piled up in the long frame time, undispersed *Chandra* image, and within $10\text{--}15''$ the knots also lie within the galaxy seen in the optical/near-IR image. However, despite this, we can make a few remarks about how the radio, optical and X-ray morphologies compare, using the short frame time data from the interleaved dataset (702798) as well as the Order 0 HETG image (dataset 703007). Knot K9’s X-ray morphology (Figure 1) has a strong peak towards its upstream end that is not seen in the radio. Unfortunately, however, it lies too close to the diffraction spike in the F160W image to fully characterize in the near-IR. Knot K14 appears to peak slightly closer to the nucleus in the radio image than in either the near-IR or X-rays. X-ray emission is clearly seen downstream of that component extending nearly continuously to knot K30. That emission is not seen in either the near-IR or the radio (the near-IR emission that is present is more likely due to subtle galaxy features in the same region, as shown in the middle panel of Figure 2). That X-ray emission includes a knot seen only in the X-rays, knot K22.

Knot K30, seen in all three bands, has an X-ray flux peak that is located significantly upstream of either the radio or near-IR one (Fig 4), with the near-IR peak lo-

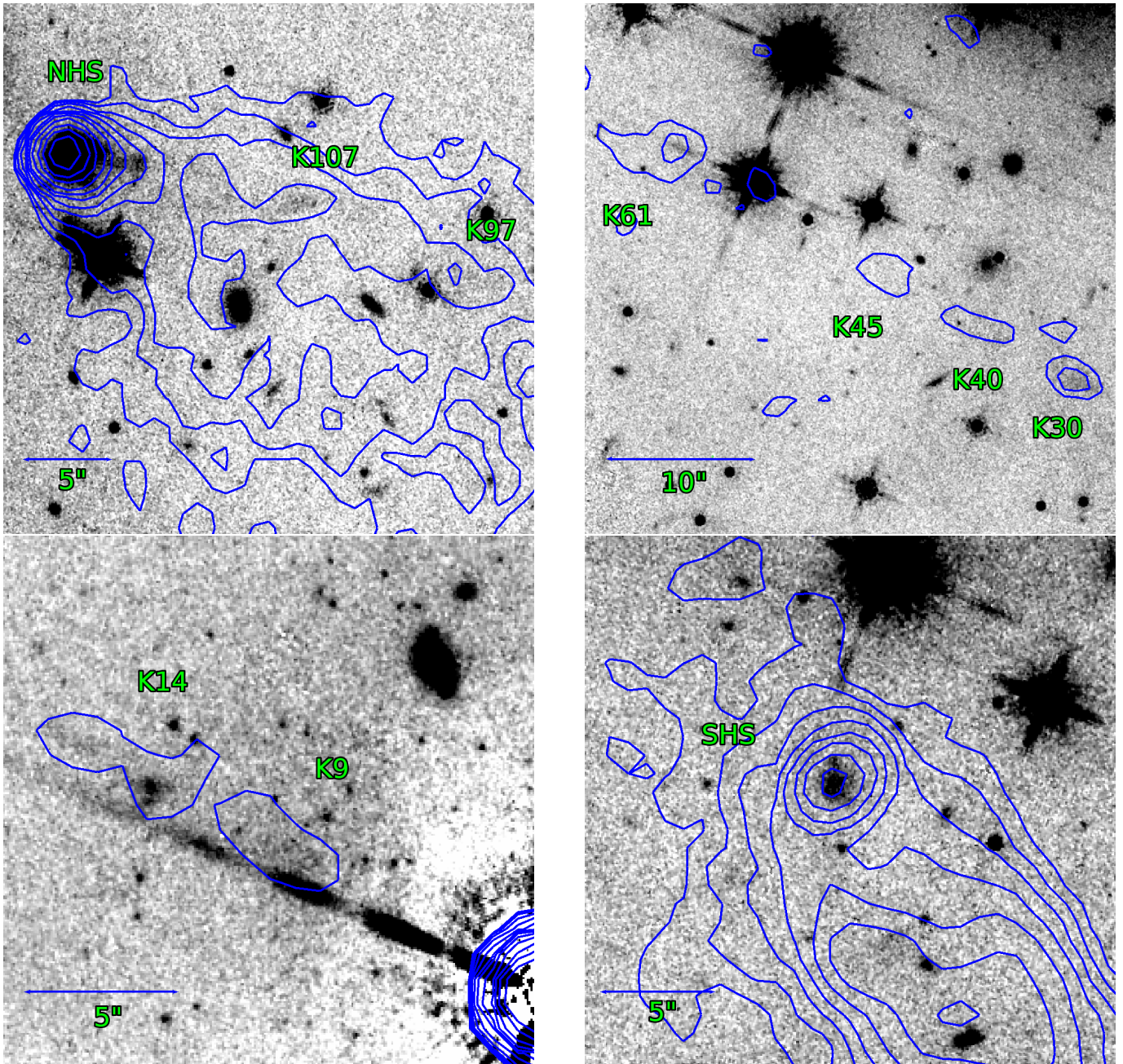


Figure 2. *HST* images of the jet of 3C 111, obtained with the WFC3/IR + F160W. All four panels show the *HST* image in greyscale, with contours from the radio image over-plotted in blue. A galaxy model has been subtracted from the *HST* image (see §3). At top left, we show the brighter, northern hotspot, which is well resolved both parallel to and perpendicular to the jet direction. The top right and bottom left images show the inner part of the northern jet, specifically the part extending from about $5''$ to about $65''$ from the nucleus. The bright linear feature in the bottom left panel is a diffraction spike. At bottom right, we show the fainter, southern hotspot, which is also well resolved. The X-ray detected knots have been labelled in green.

cated closer to the nucleus than the radio one. The X-ray flux from K30 also declines much more quickly with increasing distance from the nucleus than in either the near-IR or radio, which show similar decline rates (Figure 3). The K40-K45 region is also complex. The radio flux of K40 displays two peaks, with the near-IR peak associated with the one closer to the nucleus. The X-ray emission, however, does not peak until $42''$ from the nucleus, where there is an apparent radio minimum. The radio emission picks up again between 43 - $45''$, while through that region and extending out to nearly $50''$, the

X-ray emission appears roughly continuous and there is no significant X-ray knot at $51''$ from the nucleus as there is in the radio. Moving further out, there is a flux maximum at about $55''$ from the nucleus in the radio image that is not seen in the X-ray or F160W images. Knot K61, which represents an apparent 'kink' in the jet, is seen in both the radio and X-rays. Its X-ray morphology has a 'corkscrew' like appearance that is not prominent in the radio, where only its downstream half can be seen. In the optical/near-IR, K61 unfortunately lies very near a bright foreground star and so while there is possible

Table 2
Jet Component Flux Densities

Region	Radio mJy	F160W μ Jy	F850LP μ Jy	F791W μ Jy	2 keV nJy
K9	6.91 ± 0.30	4.88 ± 0.12	$< 8^a$	\dots^e	1.07 ± 0.20
K14	9.35 ± 0.44	5.38 ± 0.15	$< 10^a$	\dots^e	0.91 ± 0.16
K22	3.78 ± 0.42	0.46 ± 0.20	$< 11^a$	\dots^e	0.40 ± 0.11
K30	13.15 ± 0.60	8.75 ± 0.23	$\dots^{a,b}$	$< 11^a$	2.26 ± 0.26
K40	8.25 ± 0.44	2.13 ± 0.20	$< 14^a$	$< 7^a$	0.35 ± 0.09
K45	11.96 ± 0.52	1.13 ± 0.25	$< 17^a$	$< 9^a$	0.55 ± 0.11
K51	6.03 ± 0.49	1.72 ± 0.18	$< 16^a$	$< 8^a$	0.22 ± 0.08
K61	38.13 ± 0.95	1.77 ± 0.46^b	$< 22^{a,c}$	$< 23^{a,c}$	4.38 ± 0.40
K97	27.88 ± 0.42	2.01 ± 0.28	$< 11^a$	$< 6^a$	0.59 ± 0.09
K107	58.00 ± 0.51	4.70 ± 0.36	$< 16^a$	$< 12^a$	0.18 ± 0.06
NHS	610.31 ± 0.47	121.0 ± 0.6	\dots^d	44.3 ± 4.0	1.86 ± 0.21
SHS	182.52 ± 0.63	13.39 ± 0.53	$< 22^a$	\dots^e	0.35 ± 0.09

^a Flux quoted is a 2σ upper limit.

^b Located in chip gap.

^c Bright star plus diffraction spikes within region.

^d At chip border, significant part of region off chip.

^e Knot is off chip.

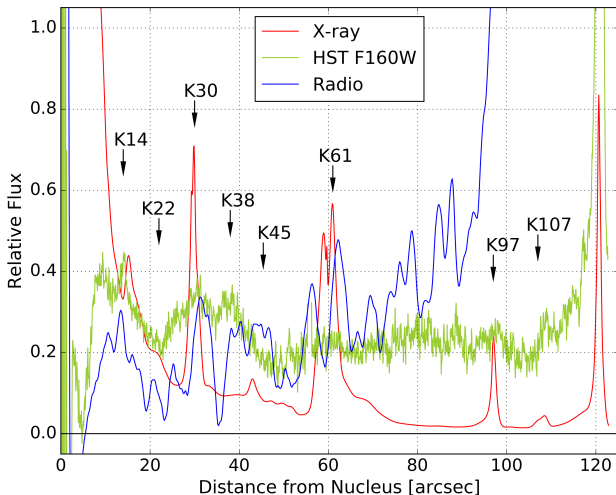


Figure 3. Relative flux as a function of distance from the nucleus for the approaching jet of 3C 111, as seen in the radio (VLA image, blue trace), near-IR (*HST/WFC3 IR/F160W* image, green trace) and X-rays (*Chandra* image, red trace). Each of the three traces was extracted from a slice $1.476''$ wide, along a vector extending from the nucleus of the galaxy through the NHS. Major knot regions are labeled above the traces. See §2 for details on the alignment of the three images, and see §3 for discussion.

emission in the near-IR it lies too close to the star or its diffraction spikes to have confidence in its detection and/or measure a flux.

Four regions are seen within the extended lobes. Within the northern lobe we see knots K97 and K107, as well as the flux maximum of the NHS itself. While these three hotspots have outwardly similar morphologies in the X-ray, near-IR and radio, close examination reveals important differences. In particular, it is only in the radio that one appreciates the extent of the northern lobe, which extends for over $30''$ in a ‘plume’ shape that includes both K97 and K107. In the X-ray and near-IR, we see only the three hotspots (with K97 barely detected), plus extensions to the NHS in two directions, the first being back upstream pointing at K107, and the second

one pointing off to the southwest parallel to the flux contours defining the lobe’s southern edge. The latter could indicate material outflowing from the hotspot, similar to what has been postulated for the 3C 273 jet by Röser et al. (1996), while the general shape of the jet in that region indicates that the jet does bend as it enters the lobe. A close look at the NHS itself also reveals that its flux maximum is not located at the same position in the radio, near-IR/optical and X-ray, with the X-ray maximum seen upstream of the maxima seen in the near-IR/optical and radio (which are aligned with each other). This misalignment, which is suggestive but not firm at the $2.5\text{-}3\sigma$ significance level, is shown in Figures 1 and 2, and quantified in Fig. 4. In addition, we also see for the first time X-ray and near-IR emission from the SHS. The radio and near-IR emission from the SHS flux are well aligned (Fig. 2), while there simply are not enough photons detected in the *Chandra* image to firm up the comparison between its X-ray and optical flux maximum position, as only 32 ± 8 counts are seen from the SHS and the X-ray emission is significantly extended.

3.2. Jet Spectral Energy Distribution

We have extracted fluxes and spectral energy distributions (SEDs) for all jet and hotspot regions. The sky regions used are shown in Figure 1 as green ellipses. The results are given in Table 2. Where a component is not detected in a given band, we give a 2σ upper limit. The optical and near-IR fluxes were extracted from the galaxy-subtracted images and are corrected for extinction using the published value of A_V . In addition, for the near-IR and optical fluxes we also subtracted the average flux from a radial ring at the same distance from the nucleus, in order to minimize galaxy subtraction residuals. This was necessary because of the rather disturbed morphology of the host galaxy as well as the presence of several bright, nearby companion galaxies as well as bright stars. To convert the optical and near-IR count rates into fluxes we used the header information from SYNPHOT. By default, these assume a flat spectrum ($\alpha \approx 0, F_\nu \propto \nu^{-\alpha}$); however, the errors from this assumption are typically $< 5\%$ in these wide bands. The fluxes in a given band are assumed to be centered at the

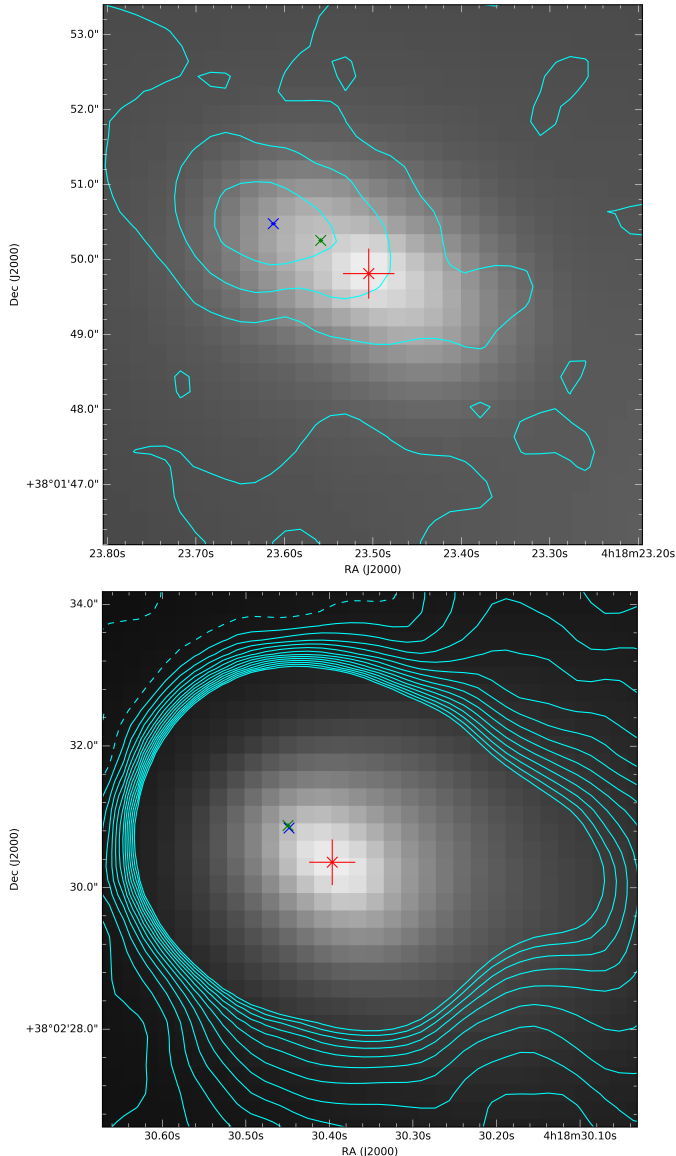


Figure 4. Close-up views of the K30 (top) and NHS (bottom) regions of the *Chandra* image, showing the location of the flux maxima in the radio (blue), near-IR (green), and X-ray (red) bands. The sizes of the error bars on each position are shown. Radio contours overlaid in cyan.

band’s pivot wavelength.

The X-ray spectra of the three brightest regions in the 3C 111 jet (knots K30 and K61, and the NHS) were extracted using *specextract*. The extraction regions used are shown on Figure 1. Background spectra were obtained using annular regions at the same radii as the components itself, and excluding the readout streak. We used unweighted ARFs and RMFs and corrected for the PSF. Spectral fitting was done in *Sherpa* using *XSpec* models *xsphabs* and *xspowerlaw*.

Determining the correct column density of absorption for 3C 111 is complicated, as it is known that the source shows an additional absorbing column in excess of the Galactic value of $N_H = 3.0 \times 10^{21} \text{ cm}^{-2}$ (e.g., Reynolds et al. (1998); Ballo et al. (2011); Tombesi et al. (2013)). For this analysis, we have used Galactic absorption with a column density of $N_H = 8.6 \pm 0.02 \times 10^{21} \text{ cm}^{-2}$. This

Table 3
Jet Component X-ray Spectra

Region	Normalization	α	χ^2_ν
K30	$4.27 \pm 0.58 \times 10^{-14}$	0.76 ± 0.29	0.944
K61	$8.28 \pm 0.82 \times 10^{-14}$	1.01 ± 0.21	0.985
NHS	$3.49 \pm 0.48 \times 10^{-14}$	0.83 ± 0.28	0.927

was determined from the *Chandra* HETG data set, the full analysis of which will be discussed in a future paper (Tombesi et al., in prep.). The other *Chandra* data sets of 3C 111 suffer from pileup in the region of the quasar nucleus, making it impossible to determine accurately the value of N_H from them – e.g., using our 0.3s frame time data to fit the absorption gives a value of $5.04 \times 10^{21} \text{ cm}^{-2}$. An N_H of $8.6 \times 10^{21} \text{ cm}^{-2}$ is consistent with previous expectations (see also Tombesi et al. (2013)).

We used the CSTAT statistic in *Sherpa* as well as the Simplex (aka Nelder-Mead) fitting optimization method because of their robustness in low-signal cases. These fits were all checked using the Monte-Carlo method, and the results matched those of Simplex. The CSTAT statistic in *Sherpa* is equivalent to the Cash statistic but allows for easier checking of the goodness-of-fit. We checked the goodness-of-fit in two ways: first, by looking at the reduced statistic; and second, by running a simulation of the model and using *plot_cdf* to check that the cumulative distribution function had a median at about 0.5. The fitting was done for 0.5–7 keV on unbinned data. The flux was determined from the *calc_energy_flux* function, over a range of 0.5 to 7 keV. Simulations were also used to determine the error in the flux value. Errors in flux are given at 68% confidence, while the error in photon index and normalization are given at 90% confidence intervals. This yielded the X-ray spectral indices given in Table 3. As can be seen, all three regions have X-ray spectral indices between $\alpha = 0.76$ to $\alpha = 1.01$. The X-ray fluxes from other jet regions were corrected for scattered light from the AGN itself using annular regions at the same radius as the component itself. The X-ray count rates for all jet regions were converted to flux assuming Galactic absorption. For the three regions where X-ray spectral fitting was possible, we used the power-law fits given in Table 3. For all other regions, we used a power-law index of $\alpha = 0.87$, equal to the average of the three regions fit.

We show the resulting SEDs for all the components in Figure 5. For regions K30, K61 and the NHS, we use the fitted X-ray flux and spectral index. Fig. 5 also includes ground-based K and R-band fluxes for the NHS that were previously published in Meisenheimer et al. (1997), corrected with updated values for the Galactic extinction (squares in the lower right panel, see discussion in §2.2), as well as a 1.3 mm flux from IRAM (Meisenheimer et al. 1989). The 1.3 mm IRAM point lies very close to the power law ($\alpha_R = 0.85$) extrapolated from the 8.4 GHz observation of Leahy et al. (1997). The apparent discrepancy between our F160W flux (Table 2, circles in Fig. 5) and the extrapolation of the K-to-R band spectral index from Meisenheimer et al. (1997) merits further discussion. We chose a slightly larger aperture than Meisenheimer et al. (1997), to include faint extended flux not seen by those authors, as shown in Figure 6. This is only 3% of the total, and both after and before

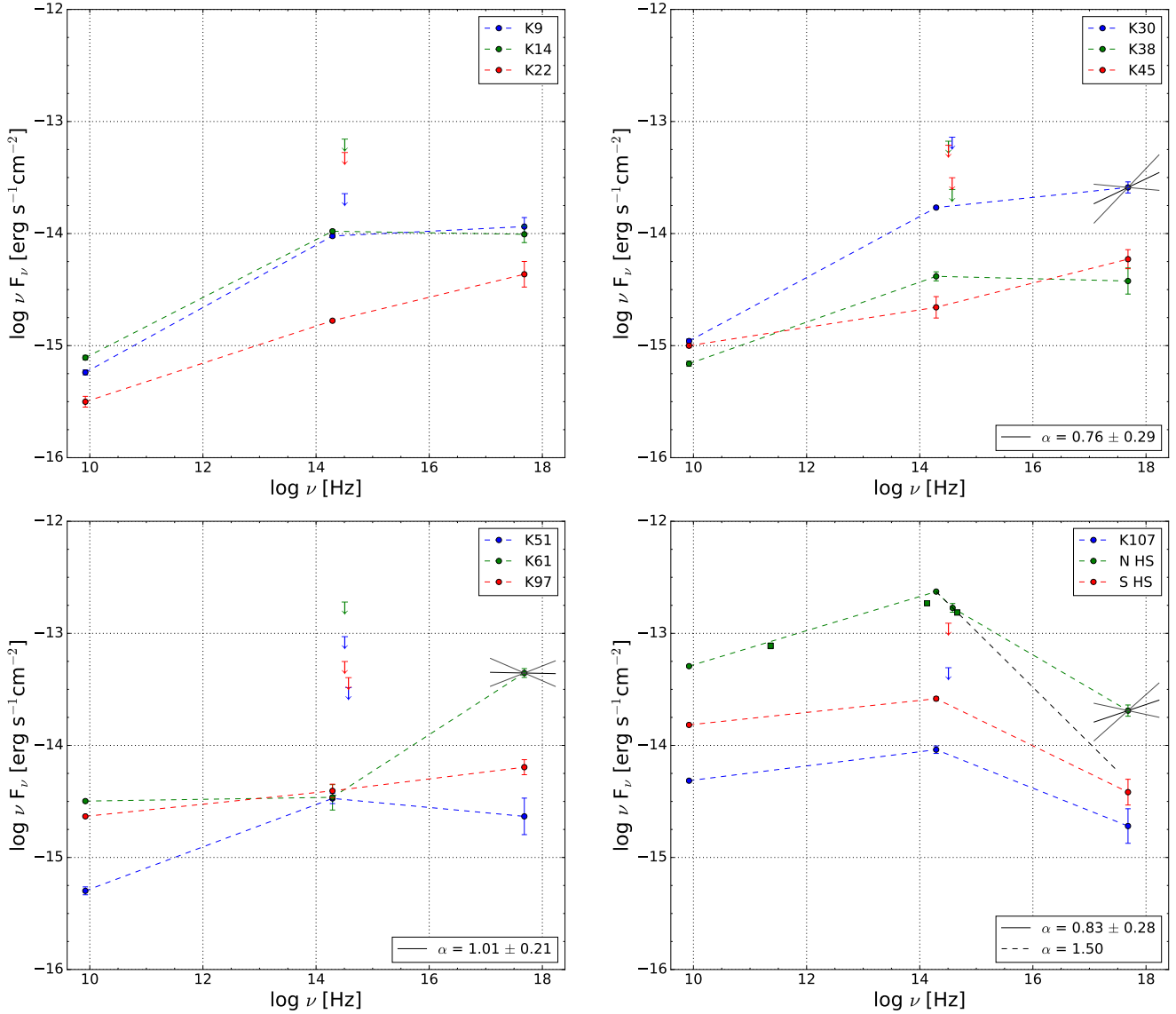


Figure 5. Spectral energy distributions for the jet and hotspot regions. We have connected all detected fluxes by simple power laws (= straight lines in these log-log plots). Where X-ray spectra are fit, these fits are indicated. In the NHS, we also plot as the black dotted line the observed near-IR to Optical spectral index. See §3.2 for discussion.

this, our F791W flux is within 1σ of the Meisenheimer et al. (1997) K to R band extrapolation. While it is possible that our flux in F160W is incorrect, we consider this unlikely given our careful choice of a source-free background region (Figure 6) and the well-established nature of the HST flux scale. Alternately, the K-band flux measurement of Meisenheimer et al. (1997) was affected by either poor background subtraction or poor flux calibration. We favor this explanation, as due to the crowded field (Figures 3, 6) it is likely that the background region in a ground-based image, like that of Meisenheimer et al. (1997), would include flux from one or more neighboring objects, thus causing an apparent underestimate of the source flux. We were unable to confirm this with the authors of Meisenheimer et al. (1997), however).

As can be seen, most of the jet components have diverse SED shapes that naively can be fit by synchrotron emission from a single electron population. For example, knots K45 and K97 appear to be fit reasonably well by

single power laws extending up to X-ray energies, and most other knots have X-ray flux that is significantly below the extrapolation of the radio-near-IR power law. However, we do not favor this simple interpretation, as in the NHS the fitted X-ray spectral slope is much harder than the extrapolation of the radio to optical synchrotron component, while in knot K61 the X-ray flux is a factor of about 4 higher than a simple extrapolation of the radio to near-IR power law. Thus a second emission component is necessary to fit the SED of these jet knots and possibly others. In broad terms, such a spectral shape has been seen before in other quasar jets (e.g., PKS 0637-752, knots WK7.8 and WK8.7, Mehta et al. 2009), and requires either a contribution from another, inverse-Compton mechanism (the so-called EC/CMB mechanism), or alternately a second, entirely distinct high-energy electron population to account for the X-ray emission. Here, however, the fitted X-ray spectra combined with the fact that the X-ray emission of knot K30 and

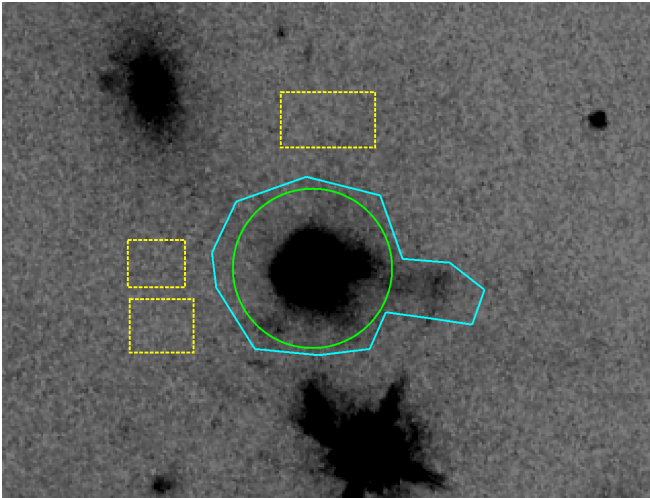


Figure 6. Close-up of the NHS region of the F160W image. The smaller region used by Meisenheimer et al. (believed to be centered on the NHS) is shown in green, while the larger region we use is shown in light blue. Our background regions are the yellow rectangles. As can be seen, the Meisenheimer et al. region did not include a small amount of extended flux from the NHS. This only makes a small difference in the flux, as we discuss in §4. However, the region is quite crowded, making the choice of the background region very sensitive. We believe that it is likely that the Meisenheimer et al. background region (dimension and location unknown) included some flux from an unrelated foreground or background source.

the NHS has a maximum at a different location than the near-IR or optical emission, makes the two-component synchrotron interpretation much more likely. Additionally, a Doppler factor of $\delta \gtrsim 45$ is required to explain the observed properties of the NHS flux if EC/CMB is the dominant emission mechanism at work (see §4.2).

4. PHYSICAL CONSIDERATIONS

The jet of 3C 111 is unique for several reasons. Chief among these are the fact that both the approaching and receding hotspots can be seen in all bands, and its extreme length, with X-ray and near-IR components seen in the jet for more than 100 arcseconds. The data we present here can be used to place a variety of constraints on both the kinematics of the jet as well as the X-ray emission mechanism. In §4.1, we use the detection of both the approaching and receding hotspots, as well as VLBA observations, to comment on the kinematics of the jet, while in §4.2 we discuss efforts to model the X-ray spectrum and broadband spectral energy distribution of the brightest knots to constrain their emission mechanism in the X-rays.

4.1. Jet Deceleration

The flux ratio between the northern and southern hotspots can be used to determine the permitted values for β and θ by using

$$\frac{S_1}{S_2} = \left(\frac{1 + \beta \cos\theta}{1 - \beta \cos\theta} \right)^{2+\alpha} \quad (1)$$

(e.g., Boettcher et al. (2012)). We do this individually for the radio, near-IR, and X-ray bands. Here, θ is the angle to the line of sight, $\beta = v/c$, and α is the spectral index for each band (0.85 for radio, 1.50 for near-IR, and 0.83 for X-ray; see Figure 5, lower right panel and discussion in §3.2). The jet/counterjet hotspot flux ratio

differs significantly between bands: 3.34 ± 0.01 in the radio, 9.03 ± 0.36 in the near-IR, and 5.34 ± 1.61 in the X-ray. This equation makes the assumptions that the jet and counterjet are exactly identical and 180° apart. Jorstad et al. (2005) used VLBA observations and determined the most likely viewing angle to be 18.1 ± 5.0 degrees on the parsec scale. We found the permitted range of β and θ for the VLBA scale by using their value for the transverse β_T apparent to solve

$$\beta_T = \frac{\beta \sin\theta}{1 - \beta \cos\theta}. \quad (2)$$

Figure 7 shows the β vs θ plot for the parsec-scale VLBA results as well as the ~ 100 kiloparsec-scale hotspots using our data. We see a clear deceleration from $\beta \sim 0.96$ at the parsec scale to $\beta \sim 0.2-0.4$ at the hotspot, with the velocity of the radio-emitting plasma significantly slower than that of the X-ray- and near-IR-emitting plasma. This is consistent with the two-component synchrotron model due to the fact that the radio- and X-ray-emitting electron populations appear to be moving at significantly different velocities, however it may require that the near-IR-emitting electrons do not occupy the entire jet cross-section, as in the simplest version of this scenario the near-IR and radio emission come from the same spectral component. Given the relatively modest beaming we find, it is interesting that no jet components are seen in the counterjet between the nucleus and SHS. Additional *HST* and *Chandra* observations are required to better constrain the near-IR spectral index and elaborate on these issues. Oh et al. (2015) more recently used VLBI observations to constrain the viewing angle of 3C 111 on mas scales to $\theta \lesssim 20$ degrees and the intrinsic velocity to $\beta \gtrsim 0.98$, in agreement with the findings of Jorstad et al. (2005). Given the large assumptions and the probable complex structure and dynamics of the hotspot regions, this analysis serves to place an upper limit on the amount of beaming in the jet. The analysis is inconsistent with a highly-beamed jet, as we would expect the jet/counterjet hotspot flux ratio to be larger if beaming were higher.

The spectral index used for the radio is based on the assumption that the slope is constant up to the near-IR. We plan to improve on this value in a future paper where we analyze JVLA observations (C, X, and Ku bands) of 3C 111. A harder spectral index for the radio would increase the likely value for β , however the offset would not be large enough to bring it into agreement with the near-IR, where the $\Delta\beta \sim 0.1$. This uncertainty does not affect the small $\Delta\beta$ between the X-ray and near-IR, though the near-IR spectral slope could change a small amount with additional *HST* bands to fit the slope.

While the viewing angle has a rather large uncertainty, the β value is much more constrained. The relative difference in β between bands is preserved no matter the viewing angle, adding to the evidence that there are two electron populations moving at significantly different speeds.

The jet to counterjet length ratio is in relatively good agreement with the radio jet to counterjet flux ratio. The approaching jet is ~ 121 arcsec in length and the counterjet is ~ 74 arcsec in length, giving a length ratio of 0.61. For a jet moving at a constant speed β and angle θ , we expect the ratio of the lengths to be equal to

$(1 - \beta \cos \theta)/(1 + \beta \cos \theta)$. This matches well with our observed value for $\theta = 18.1^\circ$, giving a value of $\beta = 0.254$ (Fig. 7), although this depends on how the approaching and receding jets decelerate (e.g., Ryle & Longair (1967)) and whether there is bending in either jet.

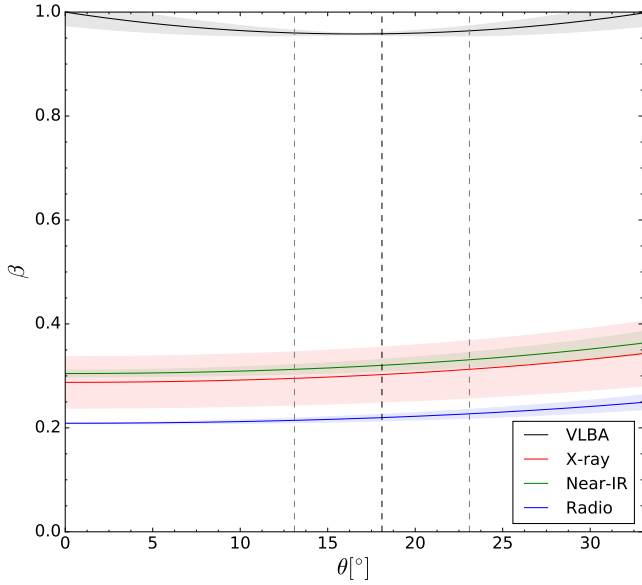


Figure 7. Plot of $\beta = v/c$ vs viewing angle for the VLBA scale (solid black line) and kpc-scale radio (blue), near-IR (green), and X-ray (red). 1σ uncertainties shown as shaded regions. The dotted lines indicate the VLBA-scale likely viewing angle of 18.1 ± 5.0 degrees.

4.2. Modeling of the Spectral Energy Distribution

The spectral indices we have obtained for K30, K61, and the NHS are all such that they must lie on either the low-energy tail or near the turnover of the second emission component. Synchrotron and EC/CMB models predict differing slopes for the emission from the very lowest energy electrons, namely $\alpha = -1/3$ for synchrotron and $\alpha = -1$ for EC/CMB (e.g., Dermer et al. (2009); Stawarz & Petrosian (2008)). If the observed spectral index at any part of the low-energy tail were to become significantly harder than $-1/3$, then that would rule out synchrotron as the dominant emission mechanism.

Figure 8 shows the spectral indices for various overlapping energy ranges. All three regions are in good agreement with constant spectral slopes across the entire 0.5-7.0 keV band.

Using the parsec-scale viewing angle of 18.1 degrees and the associated values for β from Figure 7, we can make approximations for the values of Γ and $\delta = [\Gamma(1 - \beta \cos \theta)]^{-1}$ in order to model the SED for the synchrotron and EC/CMB cases for the NHS.

Figure 9 shows several attempts at modeling the SED of K61 and the NHS with varying parameters for the synchrotron model using the Compton Sphere suite¹¹. In the case of K61, our near-IR and X-ray data serve to constrain the low-energy tail of the second emission component. However, because the near-IR spectrum for K61

¹¹ Found at <http://astro.umbc.edu/compton>

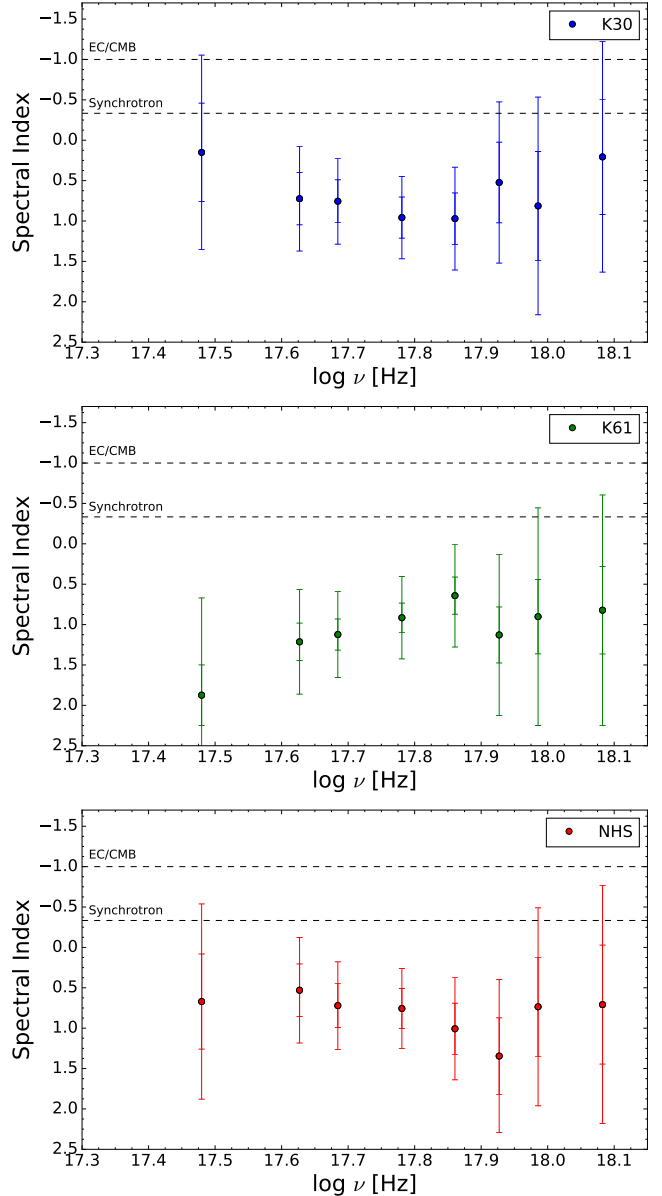


Figure 8. X-ray spectral indices for various overlapping energy ranges with error bars for 68% and 95% confidence intervals. Energy ranges: 0.5-2, 0.5-3, 0.5-3.5, 1-4, 1.5-4.5, 2-5, 2.5-5.5, 3-7 keV. The labeled dashed lines indicate the predicted spectral indices for the low-energy tail of the synchrotron and EC/CMB models.

is not available, we are not able to determine whether the detected flux is dominated by the first or second emission components – the spectrum could be either falling in the near-IR as the first synchrotron component dies off, or it could be rising as the second emission component ramps up. Future *HST* observations would allow us to constrain which emission component is responsible for the detected near-IR flux. We have plotted two example models for the second emission component showing these possibilities using a magnetic field strength ranging over $B = (1 - 3.2) \times 10^{-5}$ G, with $\gamma_{max} = (3.6 - 10) \times 10^9$, and $\gamma_{min} = (1.3 - 3.6) \times 10^7$, with a comoving luminosity of 2.15×10^{42} erg s⁻¹. The magnetic field strength B and fitted γ_{max} values translate to a radiative lifetime

of ~ 100 years, which is difficult to explain without distributed *in situ* acceleration – this requirement can be relaxed by using a lower value of B .

Varying several of the input parameters can have a large effect on the shape of the curve above 7 keV for K61 and especially in the case of the NHS. The bottom of Figure 9 shows several representative models for the SED of the NHS near the *NuSTAR* energy band. Unlike K61, the low-energy tail of the second emission component of the NHS is not constrained by the radio or near-IR data. The models shown here vary wildly in emission above 7 keV, where the magnetic field strengths ranges over $B = (0.2 - 1) \times 10^{-4}$ G, with $\gamma_{max} = (1.9 - 100) \times 10^8$, and $\gamma_{min} = (5.2 - 27) \times 10^3$, with a comoving luminosity of 1×10^{43} erg s $^{-1}$. Future observations using *NuSTAR* would allow us to constrain the SED up to ~ 80 keV.

If the X-ray emission is due only to EC/CMB, then an estimate of the magnetic field strength can be made using

$$\frac{S_{sync}}{S_{IC}} = \frac{(2 \times 10^4 T)^{(3-p)/2} B_{\mu G}^{(1+p)/2}}{8\pi\rho} \quad (3)$$

(Felten & Morrison 1966), where $\rho = \Gamma^2 \rho_0 (1+z)^4$ is the apparent energy density of the CMB at redshift z , $\rho_0 = 4.19 \times 10^{-13}$ erg cm $^{-3}$ is the local CMB energy density, the apparent temperature of the CMB is δT , and the temperature of the CMB is $T = 2.728(1+z)K$. This calculation gives a value of $B \approx 7.9 \times 10^{-5}$ G. While this is comparable to that quoted for other jets where the EC/CMB model is used to model their X-ray emission, in this case a comoving luminosity of $\sim 10^{51}$ erg s $^{-1}$ is required to fit the model to our X-ray data. We feel this is unrealistic, as it would violate the Eddington limit by many orders of magnitude. For that reason, we have not shown it in any figure.

Additionally, assuming an equipartition magnetic field, a Doppler factor of $\delta \sim 45$ is required for EC/CMB to explain the observed X-ray/radio NHS flux even for the case of $\theta = 0$ degrees using standard formulae (Harris & Krawczynski 2002). The required beaming is highly unlikely given the observed properties of the 3C 111 jet, *e.g.* the observed brightness of the SHS and the lack of obvious blazar properties.

We do not have many data points with which to constrain the model of the low-energy synchrotron component, especially in K30 and K61. We expect to be able model its SED well in a follow-up paper using JVLA observations of the jet. As well, additional *HST* and *Chandra* observations would help to better constrain the near-IR to optical and X-ray spectral indices of the components, and perhaps also constrain the X-ray emission mechanism of additional components.

5. CONCLUSIONS

We have presented new *Chandra* and *HST* observations of 3C 111 that reveal that its jet has eight X-ray and near-IR/optical emitting components, which extend for 121 arcsec (355 kpc deprojected length) from its AGN nucleus in the approaching jet, and also reveal the hotspot emission on the counterjet side. The 3C 111 jet is remarkable for several reasons. While some other jets are comparably long, no other known jet boasts the same

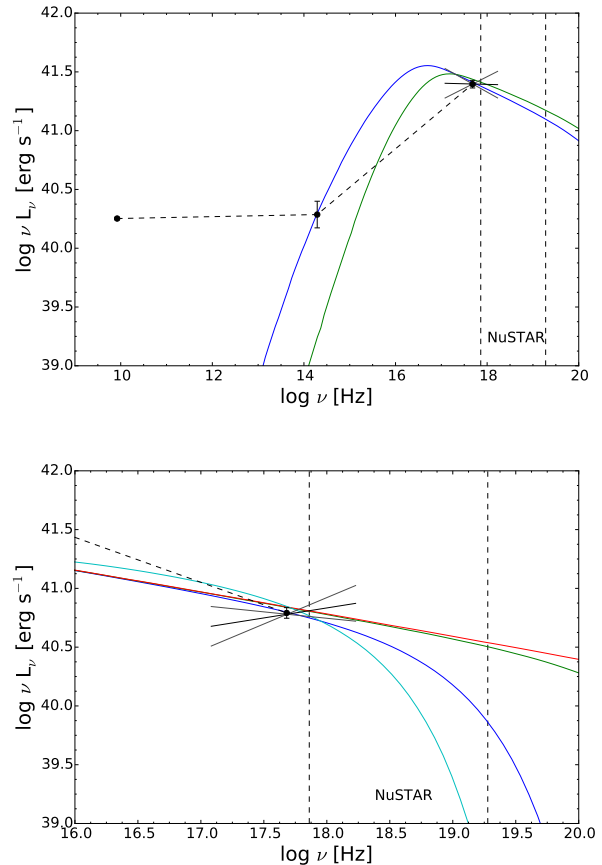


Figure 9. Representative models for the SED of the high-energy synchrotron component along with our binned X-ray data for K61 (*Top*) and the NHS (*Bottom*). Dashed vertical lines represent the boundaries of the energy range that *NuSTAR* is capable of observing.

combination of length, number of visible components and low redshift that 3C 111 does. For example, the jet of Pic A (Marshall et al. 2010; Gentry et al. 2015; Hardcastle et al. 2016), which is similarly straight, longer in angular extent (almost 4'), and is about 30% nearer, has only three components that have been detected in the near-IR, while the jet of 3C 273 (Jester et al. 2006), which extends for a somewhat greater distance from its host galaxy and is somewhat brighter, is nearly 4 \times as far at a redshift $z = 0.158$.

The analysis discussed in this paper strongly disfavors the EC/CMB model as the dominant X-ray emission mechanism in several of the components of 3C 111's jet. The hotspot flux ratio for each of the bands we have shows the jet to have decelerated to, at most, $\beta \sim 0.4$. This, combined with a relatively high viewing angle of $\theta \sim 18.1^\circ$ based on VLBA observations, demands a power requirement many orders of magnitude above the Eddington limit for EC/CMB to be the dominant X-ray emission mechanism of the jet.

We instead favor a two-component synchrotron model. Morphological comparison between radio, near-IR, and X-ray bands for K30 and the NHS show the X-ray flux maxima to be significantly upstream of the maxima in the radio, suggesting the presence of two separate elec-

tron populations with distinct energy distributions in these regions. This evidence is compounded by the analysis of the jet/counterjet hotspot flux ratio for each band, which shows the near-IR- and X-ray-emitting electrons to be moving at a significantly faster velocity than that of the radio-emitting electron population.

We have made efforts to model the spectral energy distribution of the high-energy synchrotron emission and determine how future observations using *NuSTAR* can be used to constrain the emission mechanism. Future *HST* and *Chandra* observations will allow us to put further constraints on the spectral energy distribution models for the jet components we have analyzed and test the emission mechanism of additional jet components.

These results are based on observations made by the *Chandra* X-ray Observatory (datasets 702798 and 703007) and *Hubble Space Telescope* (program 13114), as well as the Very Large Array (*VLA*, program AB534). EP, DC and FT acknowledge support for this work by the National Aeronautics and Space Administration (NASA) through Chandra awards G03-14113A (EP, DC) and G04-15103A (FT) issued by the Chandra X-ray Observatory Center, which is operated by the Smithsonian Astrophysical Observatory for and on behalf of the National Aeronautics and Space Administration under contract NAS8-03060. EP and DC also acknowledge support from HST grant GO-13114.01, which was provided by NASA through a grant from the Space Telescope Science Institute, which is operated by the Association of Universities for Research in Astronomy, Inc., under NASA contract NAS 5-26555. The National Radio Astronomy Observatory is a facility of the National Science Foundation operated under cooperative agreement by Associated Universities, Inc. This research made use of Astropy, a community-developed core Python package for Astronomy (Astropy Collaboration et al. 2013), hosted at <http://www.astropy.org>. This research also made use of APLpy, an open-source plotting package for Python hosted at <http://aplpy.github.com>.

REFERENCES

- Anderson, J., MacKenty, J., Baggett, S., & Noeske, K., 2012, http://www.stsci.edu/hst/wfc3/ins_performance/CTE/
Astropy Collaboration, Robitaille, T. P., Tollerud, E. J., et al. 2013, *A&A*, 558, A33
- Ballo, L., Braitto, V., Reeves, J. N., Sambruna, R. M., & Tombesi, F. 2011, *MNRAS*, 418, 2367
- Boettcher, M., 2012, Chapter 2, *Relativistic Jets from Active Galactic Nuclei*, Edited by M. Boettcher, D.E. Harris, and H. Krawczynski, 425 pages. Berlin: Wiley, 2012
- Burstein, D., & Heiles, C., 1982, *AJ*, 87, 1165
- Cara, M., Perlman, E. S., Uchiyama, Y., et al., 2013, *ApJ*, 773, 186
- Celotti, A., Ghisellini, G., & Chiaberge, M., 2001, *MNRAS*, 321, L1
- Dermer, C. D. & Atoyan, A. M., 2002, *ApJ*, 586, L81
- Dermer, C. D., & Atoyan, A. 2004, *ApJ*, 611, L9
- Dermer, C. D., Finke, J. D., Finke, H., Böttcher, M. 2009, *ApJ*, 692, 32-46
- Dolphin, A., 2000, *PASP*, 112, 1397
- Fanaroff, B. L., & Riley, J. M. 1974, *MNRAS*, 167, 31
- Felten, J. E., & Morrison, P. 1966, *ApJ*, 146, 686
- Gentry, E. S., Marshall, H. L., Hardcastle, M. J., et al., 2015, *ApJ*, 808, 92
- Georganopoulos, M., Perlman, E. S., Kazanas, D., McEnery, J., 2006, *ApJ*, 653, L5
- Georganopoulos, M., & Kazanas, D., 2004, *ApJ*, 604, L81
- Georganopoulos, M. & Kazanas, D., 2003, *ApJ*, 589, L5
- Gonzaga, S., Hack, W., Fruchter, A., & Mack, J., 2012, “The DrizzlePac Handbook, Version 1.0” (Baltimore: STScI)
- Güdel, M., Briggs, K. R., Arzner, K., et al., 2007, *A&A*, 468, 353
- Hardcastle, M. J., Harris, D. E., Worrall, D. M., et al., 2004, *ApJ*, 612, 729
- Hardcastle, M. J., Lenc, E., Birkinshaw, M., et al., 2016, *MNRAS*, 455, 3526
- Hardcastle, M. J., 2006, *MNRAS*, 366, 1465
- Harris, D. E., & Krawczynski, H. 2002, *ApJ*, 565, 244
- Hewitt, A., & Burbidge, G., 1991, *ApJS*, 75, 297
- Hogan, B., Lister, M. L., Kharb, P., Marshall, H. L., Cooper, N. J., 2011, *ApJ*, 730, 92
- Holtzman, J. A., Hester, J. J., Casertano, S., et al., 1995, *PASP*, 107, 156
- Jester, S., Harris, D. E., Marshall, H. L., Meisenheimer, K., 2006, *ApJ*, 648, 900
- Jorstad, S. G., Marscher, A. P., Lister, M. L., et al. 2005, *AJ*, 130, 1418
- Kharb, P., O’Dea, C. P., Tilak, A., et al., 2012, *AJ*, 748, 81
- Krawczynski, H., 2012, *ApJ*, 744, 30
- Leahy, J. P., Black, A. R. S., Dennett-Thorpe, J., et al., 1997, *MNRAS*, 291, 20
- Lister, M. L., Cohen, M. H., Homan, D. C., et al., 2009, *AJ*, 138, 1874
- Lister, M. L., Aller, M. F., Aller, H. D., et al., 2013, *AJ*, 146, 120
- Marshall, H. L., Schwartz, D. A., Lovell, J. E. J., et al., 2005, *ApJS*, 156, 13
- Marshall, H. L., Hardcastle, M. J., Birkinshaw, M., et al., 2010, *ApJ*, 714, L213
- Mehta, K. T., Georganopoulos, M., Perlman, E. S., Padgett, C. A., Chartas, G., 2009, *ApJ*, 690, 1706
- Meyer, E. T., & Georganopoulos, M., 2014, *ApJ*, 780, L27
- Meyer, E. T., Georganopoulos, M., Sparks, W. B., Godfrey, L., Lovell, J. E. J., Perlman, E. S., 2015, *ApJ*, 805, 154
- Meisenheimer, K., Röser, H.-J., Hiltner, P. R., Yates, M. G., Longair, M. S., Chini, R., Perley, R. A., 1989, *A&A*, 219, 63
- Meisenheimer, K., Yates, M. G., & Röser, H.-J., 1997, *A&A*, 325, 57
- Oh, J., Trippe, S., Kang, S., et al. 2015, *Journal of Korean Astronomical Society*, 48, 299
- Poutanen, J., & Vilhu, O. 1993, *A&A*, 275, 337
- Rajan, A., 2011, *WFC3 Data Handbook*, STScI
- Reynolds, C. S., Iwasawa, K., Crawford, C. S., & Fabian, A. C. 1998, *MNRAS*, 299, 410
- Riess, A., 2000, *WFPC2 ISR 00-04*
- Röser, H.-J., Conway, R. G., & Meisenheimer, K., 1996, *A&A*, 314, 414
- Rots, A. H., Budavari, T., 2011, *ApJS*, 192, 8
- Ryle, M., Sir, & Longair, M. S. 1967, *MNRAS*, 136, 123
- Sambruna, R. M., Gambill, J. K., Maraschi, L., 2004, *ApJ*, 608, 698
- Schwartz, D. A., Marshall, H. L., Lovell, J. E. J. et al., 2000, *ApJ*, 540, L69
- Schlafly, E. F., & Finkbeiner, D. P., 2011, *ApJ*, 737, 103
- Schlegel, D. J., Finkbeiner, D. P., & Davis, M., 1998, *ApJ*, 500, 525
- Stawarz, L., & Petrosian, V. 2008, *ApJ*, 681, 1725
- Tavecchio, F., Maraschi, L., Sambruna, R. M., Urry, C. M., 2000, *ApJ*, 544, L23
- Tombesi, F., Reeves, J. N., Reynolds, C. S., García, J., & Lohfink, A. 2013, *MNRAS*, 434, 2707
- Ungerer, V., Nguyen-Quang-Rieu, Maaron, N., Brillet, J., 1985, *A&A*, 146, 23
- van Dokkum, P. G., 2001, *PASP*, 113, 1420
- Wilson, A. S., Young, A. J., & Shopbell, P. L., 2001, *ApJ*, 547, 740